Article

Numerical Investigation of a Radially Cooled Turbine Guide Vane Using Air and Steam as a Cooling Medium

Sondre Norheim and Shokri Amzin *

Department of Mechanical and Marine Engineering, Western Norway University of Applied Sciences (HVL), Inndalsveien 28, 5063 Bergen, Norway; sondre.norheim@hotmail.com
* Correspondence:shokri.amzin@hvl.no

Abstract: Gas turbine performance is closely linked to the turbine inlet temperature, which is limited by the turbine guide vanes ability to withstand the massive thermal loads. Thus, steam cooling has been introduced as an advanced cooling technology to improve the efficiency of modern high-temperature gas turbines. This study compares the cooling performance of compressed air and steam in the renowned radially cooled NASA C3X turbine guide vane, using a numerical model. The conjugate heat transfer (CHT) model is based on the RANS-method, where the shear stress transport (SST) $k-\omega$ model is selected to predict the effects of turbulence. The numerical model is validated against experimental pressure and temperature distributions at the external surface of the vane. The results are in good agreement with the experimental data, with an average error of 1.39% and 3.78%, respectively. By comparing the two coolants, steam is confirmed as the superior cooling medium. The disparity between the coolants increases along the axial direction of the vane, and the total volume average temperature difference is 30 K. Further investigations are recommended to deal with the local hot-spots located near the leading- and trailing edge of the vane.

1. Introduction

Growing awareness of global warming and stringent regulations has led to a shift in the global energy market towards renewable energy such as solar, wind and hydropower. Although renewable energy production is increasing, it still accounted only for 14% of the global energy market in 2019 compared to fossil fuels, approximately 80% [1]. Therefore, it is improbable that renewable energy would replace fossil fuels soon. Thus, to reduce the environmental impact, it is necessary to improve the efficiency of the already existing combustion systems.

One of the most widely adopted combustion systems is the gas turbine, which plays a preeminent role in aviation and energy production [2,3]. The gas turbines provide continuous combustion and follow the Brayton cycle [4]. The cycle involves isentropic (constant entropy) compression and expansion and isobaric (constant pressure) heat addition and rejection. The actual cycle involves further losses like mechanical, aerodynamical, heat release, and pressure drop, reducing the gas turbine efficiency and increasing environmental impacts. Hence, these losses must be minimised.

Among the most influential parameters that affect the efficiency is the turbine inlet temperature (TIT) [5]. This temperature is constrained by the turbine vanes and blades ability to withstand the arduous operating conditions. These components are pushed to the limit of what the materials can endure in modern gas turbines, withstanding temperatures exceeding 1700 °C [6,7]. Thus, sophisticated cooling techniques are required to ensure that the blades and vanes can function under the immense thermal loads [8,9]. For instance, minor variations in the inlet temperature could significantly impact the lifespan of these components [10]. Therefore, it is critical to have adequate tools to predict the heat transfer mechanism in the vanes so that the design can be optimised.

Due to the complexity of gas turbines, it is challenging to obtain experimental results on these effects. Hylton et al. [11,12] were able to investigate this phenomenon; the other alternative would be computational fluid dynamics (CFD). Unlike expensive experimental investigations, CFD can provide detailed approximations of complex fluid flows with a reasonable computational cost. With the recent advancements in computer power, CFD has become more accurate, making it an indispensable tool for solving heat transfer problems.

Conjugate heat transfer (CHT) analysis is frequently used in CFD to predict the heat transfer mechanism between the hot gases and materials. The CHT couples interact between the conduction (solid body) and the convection (fluid flow). A coupled aerodynamic and thermal numerical approach for gas turbines was developed by Bohn et al. [13,14] in the early 1990s. Using the exact discretisation and numerical scheme for both the fluid flow and the solid body, the heat flux between the two regions becomes interchangeable. Thus, information about heat transfer coefficients on the solid surface is irrelevant, and the temperature distribution in the solid is a direct result of the analysis. The CHT approach has been used to validate 3D computations on the NASA C3X vane [15]. A comparison of conjugate and nonconjugated heat transfer has been performed [16], and a decoupled approach has been explored [17]. Subsequently, the CHT method has been established as an essential tool for turbomachinery optimisation and design purposes.

The famous NASA C3X turbine guide vane [11] has been used in numerous studies to investigate different cooling techniques. It has been proved that the location, cross-section and mass flow rate of the cooling arrangements are highly influential on the temperature distribution in the vane [18]. Other studies have included thermal barrier coating, the effects of turbulence intensity and material selection [19,20]. Recent developments have suggested replacing compressed air with steam because of its superior heat transfer capabilities. In combined-cycle power plants, steam is easily accessible through the secondary steam turbine, which could be used on closed-loop cooling systems. As a result, the turbine efficiency is increased and also overall combined-cycle thermal efficiency is enhanced. The primary objective of this study is to investigate the effects of replacing compressed air with steam as a coolant in a turbine guide vane.

2. Mathematical Model

In this study, the fluid conjugate flow and heat transfer calculations are performed by the commercial software Simcenter STAR CCM+. The code uses the finite volume approach to solve the Reynolds-averaged Navier–Stokes (RANS) equations with the associated boundary conditions. The Favre-averaged governing equations are derived from three conservational laws; conservation of mass, momentum and energy [21]. These equations are as follows.

$$\frac{\partial \bar{\rho}}{\partial t} + \frac{\partial}{\partial x_i}(\bar{\rho}\tilde{u}_i) = 0 \tag{1}$$

$$\frac{\partial}{\partial t}(\bar{\rho}\tilde{u}_i) + \frac{\partial}{\partial x_j}(\bar{\rho}\tilde{u}_i\tilde{u}_j) + \frac{\partial \bar{p}}{\partial x_i} = \frac{\partial}{\partial x_j}(\tilde{\tau}_{ij} + \tau_{ij}^T) \tag{2}$$

$$\frac{\partial}{\partial t}(\bar{\rho}\tilde{E}) + \frac{\partial}{\partial x_i}(\bar{\rho}\tilde{u}_i\tilde{E}) + \frac{\partial}{\partial x_i}(\tilde{u}_i\bar{p}) = -\frac{\partial}{\partial x_i}(\tilde{q}_i + q_i^T) + \frac{\partial}{\partial x_j}\tilde{u}_i(\tilde{\tau}_{ij} + \tau_{ij}^T). \tag{3}$$

The $(\bar{\cdot})$ operator represents a Reynolds operator (time-average), while the $(\tilde{\cdot})$ denotes the density weighted flow variables. The variables, ρ, u, p and E represents the density, velocity, pressure and the total energy of a fluid, respectively. The term $\tilde{\tau}_{ij}$ is the shear stress tensor and is expressed by

$$\tilde{\tau}_{ij} = 2\mu\widetilde{S}_{ij} - \frac{2}{3}\mu\delta_{ij}\widetilde{S}_{kk}, \tag{4}$$

where μ is the dynamic viscosity, and δ_{ij} is the Kronecker delta. $\widetilde{S}_{ij}$ is the rate of strain tensor and is written as

$$\widetilde{S}_{ij} = \frac{1}{2}\left(\frac{\partial \widetilde{u}_i}{\partial x_j} + \frac{\partial \widetilde{u}_j}{\partial x_i}\right). \tag{5}$$

The heat flux, $\widetilde{q}_i$, is expressed by Fourier's law of conduction [22]

$$\widetilde{q}_i = -C_p \frac{\mu}{Pr} \frac{\partial \widetilde{T}}{\partial x_i}, \tag{6}$$

where C_p is the specific heat capacity, T is the temperature and Pr is the dimensionless Prandtl number. The expression for the turbulent stress tensor τ_{ij}^T, and the turbulent heat flux q_i^T, bear some resemblance to Equations (4) and (6) but do have some decisive differences.

$$\tau_{ij}^T = -\overline{\rho u_i'' u_j''} = 2\mu_t \widetilde{S}_{ij} - \frac{2}{3}\bar{\rho} k \delta_{ij} \tag{7}$$

$$q_j^T = C_p \overline{\rho u_j'' T} = -C_p \frac{\mu_t}{Pr_t} \frac{\partial \widetilde{T}}{\partial x_j} \tag{8}$$

The turbulent viscosity μ_t is estimated using turbulence models, while the turbulent Prandtl number Pr_t is usually assumed to be constant [23].

Turbulence Modelling

In RANS methodology, it is crucial to employ turbulence models to anticipate the turbulent flow pattern, and several different models have been developed to provide accurate approximations of the turbulent flow. The $k - \epsilon$ model [24] and the $k - \omega$ model [25] are two of the most popular turbulence models in CFD. Both models have some limitations when applied to CHT simulations in turbomachinery. The $k - \epsilon$ model is inadequate for separated flows (e.g., airfoils), while the $k - \omega$ model is very sensitive to inlet- and free-stream boundaries [26].

To address these issues, Menter [27] developed the shear stress transport (SST) $k - \omega$ model. The model adds an additional cross-diffusion term, which contains the scalar product of the turbulent kinetic energy k, the specific dissipation rate ω, and a blending function that incorporates the cross-diffusion term far from the walls but not near the walls. As a result, the model behaves as $k - \epsilon$ in the free-stream and $k - \omega$ near the walls. Consequently, the SST $k - \omega$ model is frequently used in simulations containing flow separation and large pressure gradients. Zheng et al. [28] compared the commercially available turbulence models against the experimental results by Hylton et al. [11], and the conclusion presented the $SST k - \omega$ turbulence model [27] as the most accurate; hence it is the selected model for this study.

The turbulent viscosity μ_t is calculated from

$$\mu_t = \rho k I, \tag{9}$$

where k is the turbulent kinetic energy and I represents the turbulent time scale which is expressed as

$$I = min\left(\frac{\alpha^*}{\omega}, \frac{a_1}{SF_2}\right), \tag{10}$$

where ω denotes the specific dissipation rate, S is given by Equation (5), and both α^* and a_1 are model coefficients. F_2 is a blending function which is calculated as

$$F_2 = tanh\left(\left(max\left(\frac{2\sqrt{k}}{\beta^* \omega d}, \frac{500\nu}{d^2 \omega}\right)\right)^2\right) \tag{11}$$

where β^* is a coefficient, d is the wall distance, and ν is the kinematic viscosity. The transport equations for the turbulent kinetic energy k and the specific dissipation rate ω are

$$\frac{\partial}{\partial t}(\rho k) + \frac{\partial}{\partial x_i}(\rho k u_i) = P_k - \rho \beta^* k \omega + \frac{\partial}{\partial x_i}\left[(\mu + \sigma_k \mu_t)\frac{\partial k}{\partial x_i}\right] \tag{12}$$

$$\frac{\partial}{\partial t}(\rho \omega) + \frac{\partial}{\partial x_i}(\rho \omega u_i) = P_\omega - \rho \beta \omega^2 + \frac{\partial}{\partial x_i}\left[(\mu + \sigma_\omega \mu_t)\frac{\partial \omega}{\partial x_i}\right]. \tag{13}$$

β^*, β, σ_k and σ_ω are model coefficients, while the two production terms, P_k and P_ω are expressed as

$$P_k = min\left(\tau_{ij}\frac{\partial u_i}{\partial x_j}, 10\beta^*\rho k\omega\right) \tag{14}$$

$$P_\omega = \gamma \rho S^2 + 2\rho(1 - F_1)\frac{\rho \sigma_{\omega 2}}{\omega}\frac{\partial k}{\partial x_j}\frac{\partial \omega}{\partial x_j}. \tag{15}$$

Equations (14) and (15) contain the additional coefficients γ and $\sigma_{\omega 2}$. The term F_1 is another blending function defined as

$$F_1 = tanh\left(\left[min\left(max\left(\frac{\sqrt{k}}{0.09\omega d}, \frac{500\nu}{d^2\omega}\right), \frac{2k}{d^2 CD_{k\omega}}\right)\right]^4\right), \tag{16}$$

where $CD_{k\omega}$ represents the cross-diffusion coefficient. All the coefficients and their formulations as summarised in Table 1.

Table 1. Model coefficients.

a_1	0.31	σ_k	$F_1\sigma_{k1} + (1 - F_1)\sigma_{k2}$
α^*	$F_1\alpha_1^* + (1 - F_1)\alpha_2^*$	σ_{k1}	0.85
α_1^*	1	σ_{k2}	1
α_2^*	1	σ_ω	$F_1\sigma_{\omega 1} + (1 - F_1)\sigma_{\omega 2}$
β^*	$F_1\beta_1^* + (1 - F_1)\beta_2^*$	$\sigma_{\omega 1}$	0.5
β_1^*	0.09	$\sigma_{\omega 2}$	0.856
β_2^*	0.09	γ	$F_1\gamma_1 + (1 - F_1)\gamma_2$
β	$F_1\beta_1 + (1 - F_1)\beta_2$	γ_1	$\frac{\beta_1}{\beta^*} - \sigma_{\omega 1}\frac{k^2}{\sqrt{\beta^*}}$
β_1	0.075	γ_2	$\frac{\beta_2}{\beta^*} - \sigma_{\omega 2}\frac{k^2}{\sqrt{\beta^*}}$
β_2	0.0828	-	-

3. Experimental Details

In this study, one of the two aerothermodynamic investigations presented by Hylton et al. [11] is used to validate the numerical model. The objectives of the original report were to acquire experimental data to verify the results of a 2D heat transfer modelling technique. In the original experiments, three C3X turbine guide vanes are located in a free stream. The centre vane is subjected to evaluation, while the two adjacent slave vanes are included to ensure steady-state aerodynamic conditions. The test vane is convectively cooled by ten radial cooling passages from the hub to the shroud. The passages have circular cross-sections and are supplied with air from individual metered lines. The geometric configuration of the vane is adopted from the experimental report [11], where the constant cross-section is located in the x-y plane, as shown in Figure 1. The height of the vane is 76.2 mm, and it has no twist. It is observed that the cooling holes are arranged according to the curvature of the centerline, except the holes near the leading edge. The geometrical specifications of the vane are summarised in Table 2.
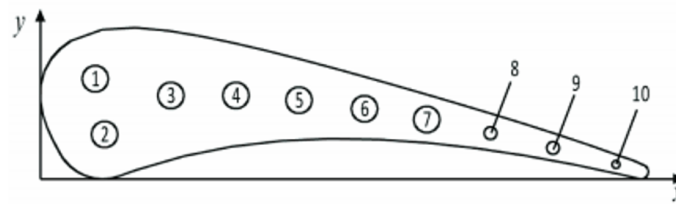
Figure 1. Schematic of the NASA C3X vane with enumerated cooling channels, as reported in the original report [11].

Table 2. Geometric parameters of C3X vane.

Setting angle (°)	59.89
Air exit angle (°)	72.38
Throat (mm)	32.92
Vane height (mm)	76.2
Vane spacing (mm)	117.73
True chord (mm)	144.93
Axial chord (mm)	78.16

The test section contains turbulence augmentation rods, followed by static pressure taps, located 187.2 mm from the leading edge of the vanes. The next exit static pressure taps are located 90.2 mm from the leading edge. The walls are cooled using steam to prevent heat radiation and keep the temperature similar to the vane surface temperature. Therefore, the walls are considered to be adiabatic. The inlet of the computational model coincides with the inlet pressure taps. The outlet is located further downstream to eliminate the effects of turbulence. Due to periodicity, the mainstream is restrained by two planes separated by 117.73 mm in the y-direction, which follows the centre-curvature of the vane. This will also reduce the computational demand of the simulations. To ensure fully developed flow and eliminate unwanted effects, such as reversed flow, both the inlet and outlet of the cooling channels are extruded 50 mm. A schematic of the computational models with boundaries is shown in Figure 2.
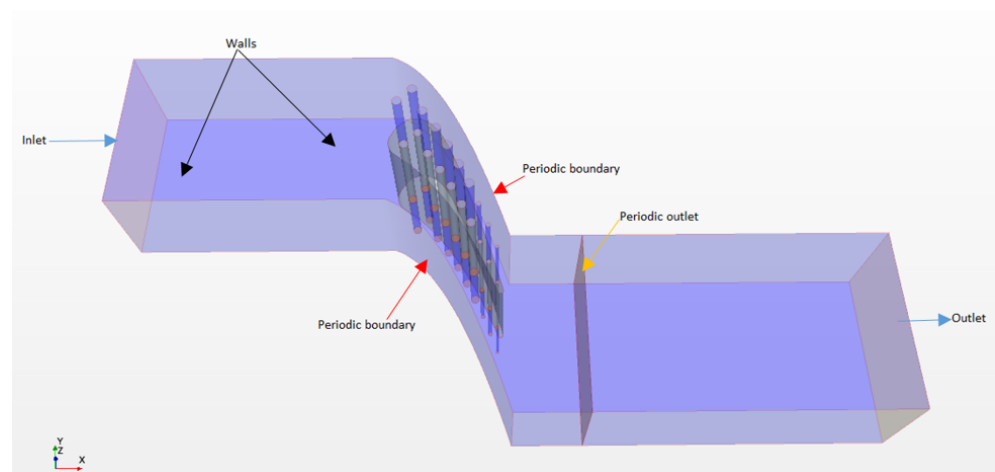
Figure 2. Computational domain.

The experimental data were obtained in the original study by instrumenting the test vane with approximately 80 thermocouples and 30 static pressure taps. The thermocouples were located at a plane near the midspan of the vane and were placed in 0.58 mm deep radial grooves. The grooves were then covered by cement and blended by hand to ensure a smooth surface. To minimise the errors from the grooves, the vane was made of ASTM310 type stainless steel, with a relatively low thermal conductivity. Similarly to the

thermocouples, the static pressure taps are mounted near the midspan. The distribution of the pressure taps is denser near the leading edge to adequately capture the large pressure gradients in this area. The installation of the pressure taps was performed similarly to the thermocouples. Each of the cooling channels was instrumented with thermocouples and static pressure taps at the inlet and the outlet. The temperature measurements on the vane surface are specified as a well-developed technique, with a proclaimed uncertainty of ± 1 °C. The free-stream temperature measurements had a reported uncertainty of ± 11 °C, due to the fluctuations from the facility combustor. As a result, the calculations of the heat transfer coefficients are severely affected by this. The pressure measurements were described with an uncertainty of ± 0.7 kPa.

4. Computational Details

4.1. Boundary Conditions

To validate the numerical model, the boundary conditions imposed on the external gas stream and the internal cooling channels are set according to code 4521, run no. 157 from the original experiments [11]. The inlet of the external gas stream is defined as a stagnation inlet to assign the boundary with uniform total pressure (P_{Tin}) and total temperature (T_{Tin}) conditions. The outlets of the gas stream and the cooling channels are defined as pressure outlets to impose static pressure (P_{Sout}) conditions at these boundaries. The inlets of each cooling channel are prescribed as mass flow inlet, with a fixed mass flow rate ($\dot{M}_{in}$) and constant static temperature (T_C) specified at each boundary. Besides, the turbulence intensity (I_u) and viscosity ratio (I_v) is fixed at the inlet of the external gas stream, while turbulence intensity (I_u) and hydraulic diameter (D_h) is specified at the inlet of each cooling channel. The details of the boundary conditions of the external gas stream are given in Table 3. The boundary conditions for the cooling channels are shown in Table 4 and are used for both the air and steam simulations.

Table 3. Boundary conditions of the external gas stream.

P_{Tin} (Pa)	T_{Tin} (K)	P_{Sout} (Pa)	I_u (%)	I_v
413,286	818	254,172	8.3	30

Table 4. Boundary conditions of the cooling channels.

Channel Number	$\dot{M}_{in}$ (g/s)	T_C (K) [28,29]	D_h (mm)	I_u (%)
1	22.2	342	6.3	10
2	22.1	344	6.3	10
3	21.8	335	6.3	10
4	22.8	336	6.3	10
5	22.5	330	6.3	10
6	22.5	355	6.3	10
7	21.6	336	6.3	10
8	7.44	350	3.1	10
9	4.77	377	3.1	10
10	2.56	387	1.98	10

The solid vane is made of ASTM type 310 stainless steel, with a relatively low thermal conductivity. The density (ρ) and the specific heat capacity (C_P) is reported as constant over the range of temperatures applicable for this study [30]. The values are set as 8030 kg/m³ and 502 J/kg·K, respectively. The thermal conductivity is assumed to vary linearly with temperature and is expressed as

$$k = 0.0115 \cdot T + 9.9105 \ (\text{W/m} \cdot \text{K}). \tag{17}$$

Both the external hot gas and the coolant gas is assumed to be operating under ideal gas conditions. Sutherland's formula [31] is used to describe the temperature-dependent dynamic viscosity (μ) and thermal conductivity (k_g), which are given by

$$\mu(T) = \mu_0 \left(\frac{T}{T_0}\right)^{3/2} \cdot \frac{T_0 + M}{T + M}, \tag{18}$$

$$k_g(T) = \lambda_0 \left(\frac{T}{T_0}\right)^{3/2} \cdot \frac{T_0 + S}{T + S}, \tag{19}$$

where the constants are represented in Table 5. Considering that the working pressure and temperature of the cooling channels are relatively low, steam is assumed to be subjected to ideal gas conditions [32]. The dynamic viscosity and thermal conductivity of steam is reported with a error of 2–4% within the working range of the simulations [33].

Table 5. Sutherland constants for air and steam [33].

Constant	Air	Steam
μ_0 (Pa×S)	1.7894×10^{-5}	1.12×10^{-5}
T_0 (K)	273.11	350
M (K)	110.56	1064
λ_0 (W/m·K)	0.0216	0.0181
S (K)	194	220

The specific heat capacity (C_p) of both cooling mediums is described by a polynomial temperature dependence, which is expressed as

$$C_p = a_0 + a_1 T + a_2 T^2 + a_3 T^3 + a_4 T^4, \tag{20}$$

where the constants are given in Table 6.

Table 6. Constants for polynomial specific heat capacity [34].

| Constant	Air	Steam
a_0	957.110256	1563.077
a_1	0.2365234	1.603755
a_2	5.141114×10^{-6}	-0.002932784
a_3	$-3.3917446 \times 10^{-9}$	3.216101×10^{-6}
a_4	$-6.0929646 \times 10^{-12}$	-1.156827×10^{-9}

4.2. Meshing

In this study, an unstructured mesh is generated in the fluid domain, the cooling channels, and vanes. At first, a polygonal surface grid is generated on the different 2D-planes, which is then stretched across the volume to create the other domains for the simulations. The outcome of this operation is a volume mesh consisting of polyhedral elements. Compared to a tetrahedral mesh, a polyhedral mesh requires about four times fewer cells for the same base size and is more numerically stable, thus reducing the computational cost of the simulations [35]. Besides, the generation of conformal grids is easier for polyhedral elements relative to hexahedral elements. The importance of conformal grids is particularly essential for CHT simulations, where information is exchanged between boundaries. Consequently, a primarily polyhedral mesh is used in this study.

To fully resolve the near-wall flow behaviour, the cells adjacent to the solid boundaries need to be fine enough to capture the boundary layer of the flow. As a result, prism layers are generated near the fluid/solid boundaries of the mesh. The total height of the prism layer should be equal to or higher than the boundary layer. In order to determine the height

of the prism layers, the dimensionless wall distance y^+ is introduced [36]. This parameter is expressed as

$$y^+ = \frac{yu_\tau}{\nu},$$ (21)

where y is the absolute distance from the wall, u_τ is the friction velocity, and ν is the kinematic viscosity. To fully resolve the boundary layer, the height of the first cell should be within the viscous sublayer, where $y^+ < 5$ [37,38]. A schematic of the mesh used in this study is shown in Figure 3, where a detailed representation of the prism layers near the boundaries is included. To save computational resources, prism layers were not applied on the adiabatic walls and periodic planes. For the same reason, the extruded regions of the mainstream and the cooling channels consist of hexahedral elements.
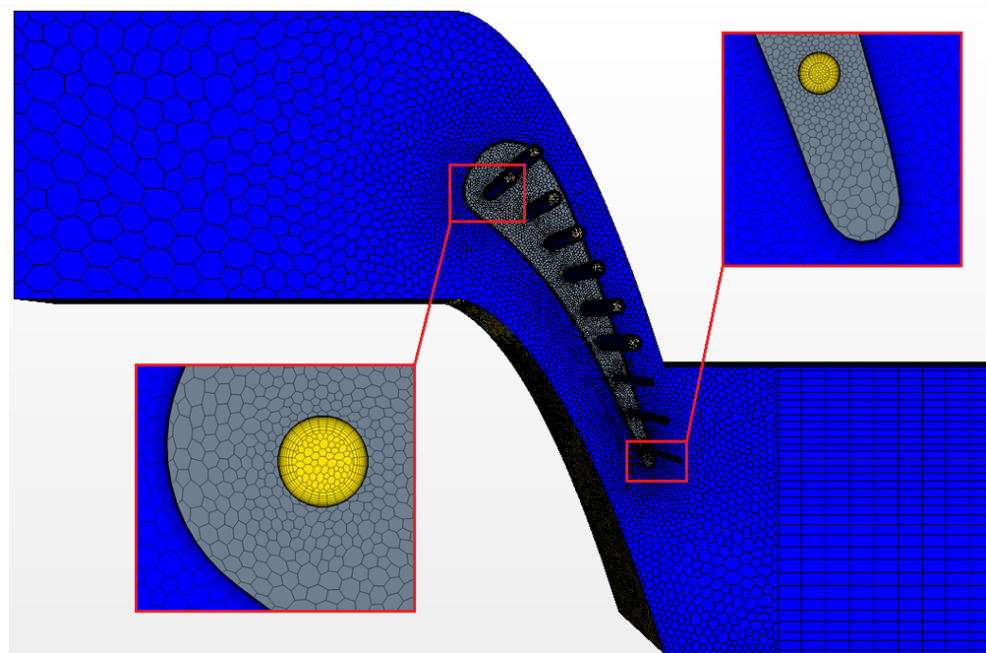
Figure 3. Schematic of the generated mesh in the X-Y plane, with detailed representation of the leading and trailing edge of the vane.

To determine if the mesh is sufficient, a mesh independence test is performed. The motivation for this test is to show that the mesh resolution does not influence the results from the simulations. The results from the mesh independence test are presented in Figure 4.
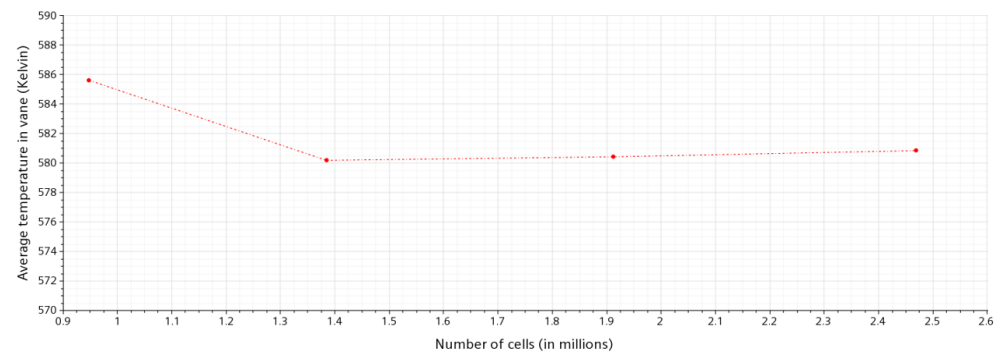
**Figure 4.** Mesh independence test.

As shown in Figure 4, six different mesh densities are tested under the same conditions. The parameter used for comparison is the maximum temperature that arises in the vane. The results show that mesh independence is achieved at approximately 1.4 million

cells. In fact, the difference between the results is less than 0.5% after this point. To save computational resources while keeping a decisive accuracy, the mesh containing 1.9 million cells is selected for further investigations, as shown in Figure 3.

5. Model Validation

To assess if the results generated by the computational model is reliable, a comparison against the experimental results by Hylton et al. [11] is performed. The dimensionless location X/L is used to show the position on the external wall of the vane. It is derived from the x-coordinate of the data points (X) and the axial chord length (L). The dimensionless location is also used to differentiate the pressure side (PS) and the suction side (SS). The leading and the trailing edges are represented by $X/L = 0$ and $X/L = 1$ or -1, respectively. The pressure and temperature distribution is normalised by P/P_{ref} and T/T_{ref}, using the reference values reported in [11].

The static pressure distribution at mid-span is used to compare the aerodynamic characteristics of the vane. It is observed that the numerical results on the pressure side $-1 < X/L < 0$ are in excellent agreement with the experimental results, as shown in Figure 5. On the pressure side, it is observed that the pressure declines slowly until $X/L = -0.5$, and then it drops drastically. When the flow is approaching the trailing edge ($X/L = -1$), the static pressure begins to fluctuate. The more complex flow behaviour leads to discrepancies between the experimental and numerical results on the suction side. From the leading edge, the flow is accelerated on the suction side. In the region where X/L is between 0.3 and 0.7, the numerical model overpredicts the acceleration. This anomaly could be explained by the turbulence model ability to consider all the complex flow phenomenon, particularly for flows with strong acceleration. However, the numerical results are still in overall good agreement with the experimental results, with an average error of 1.39%.
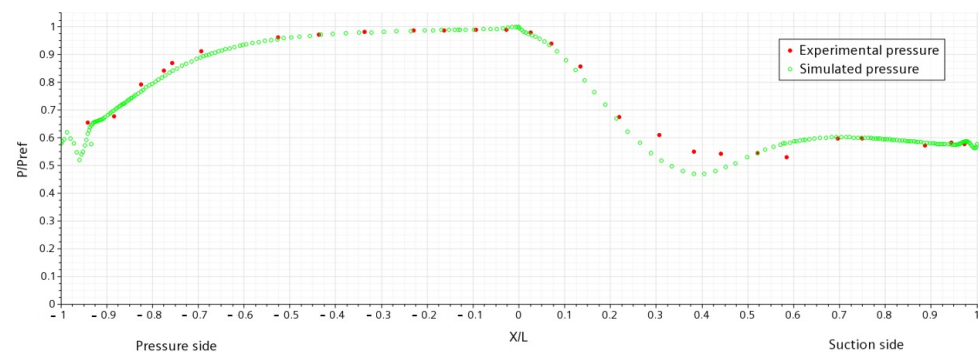

Figure 5. Comparison of the normalised static pressure from the experimental report and the numerical simulations at mid-span. The reference pressure is 413,286 Pa, as reported in [11].

Figure 6 shows the normalised temperature at mid-span and is used to validate the thermal effects of the flow. It is recognised that the predicted temperature on the pressure side is slightly overpredicted but is in alignment with the experimental results. From the leading edge, the temperature is decreasing steadily until $X/L = -0.5$. After this point, the temperature is increasing but is suffering from some local drops. These drops coincide with the position of the cooling channels, which are increasingly influential when the thickness of the vane is decreasing. As expected, the maximum temperature appears around the trailing edge, where the thickness is slim. Similarly to the pressure distribution, the temperature on the suction side of the vane is showing a clear distinction between the numerical results and the experiment, especially when X/L is between 0.1 and 0.6. Nevertheless, the two results are in good agreement with an average relative difference of 3.78%.
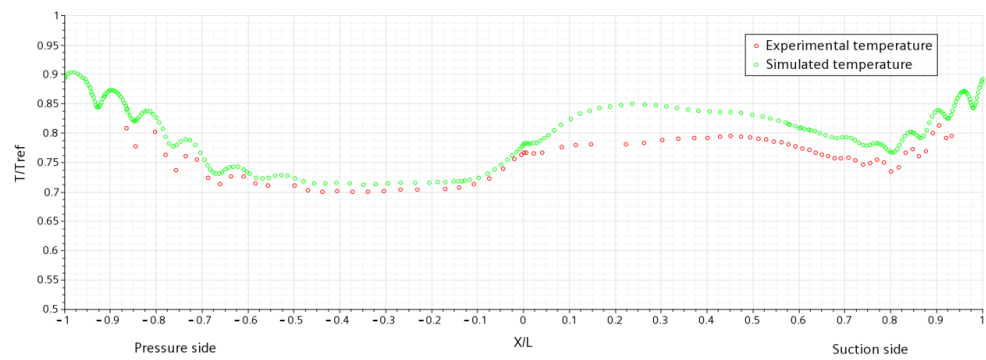
Figure 6. Comparison of the normalised temperature from the experimental report and the numerical simulations at mid-span. The reference temperature is 811 K, as reported in [11].

In order to obtain a better understanding of the discrepancies, a figure displaying the contours of the Mach number at the mid-span plane is presented in Figure 7. It is observed that the flow splits at the leading edge, which is followed by an acceleration on both sides of the vane. On the pressure side, the Mach number increases gradually toward the trailing edge, causing the static pressure to decrease. Near the trailing edge, a sudden surge of the Mach number occurs, which increases the velocity. The flow is then reunited as it passes the trailing edge, causing the reduction of the mach number.
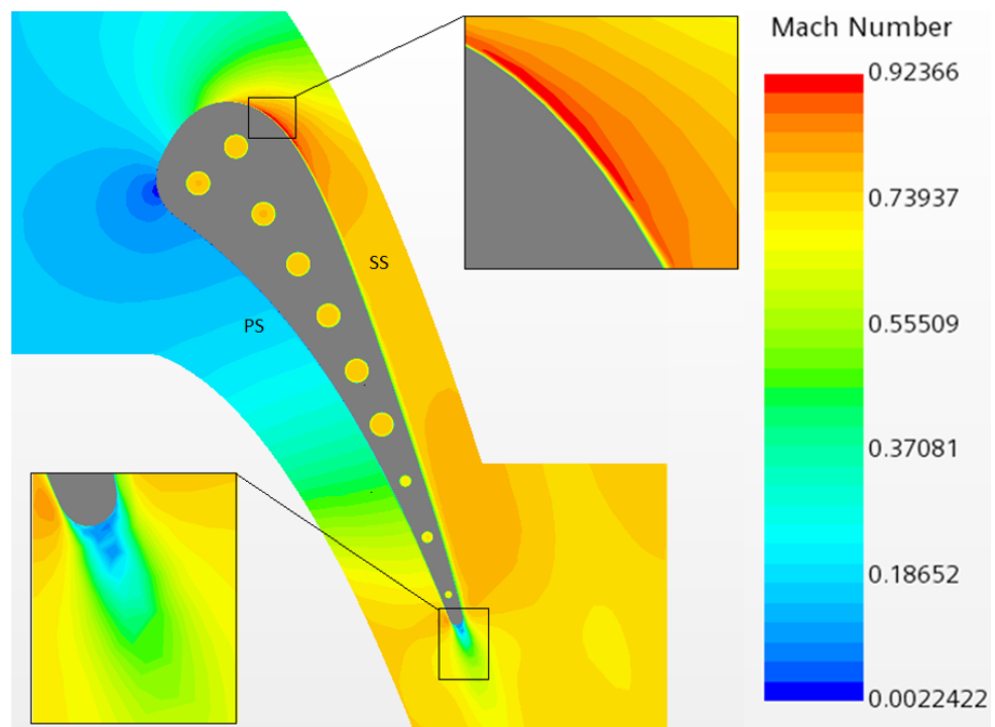

Figure 7. Contours of the Mach number on the mid-span plane, including enlarged views of the transition regions on the suction side and near the trailing edge.

On the suction side, the flow accelerates rapidly toward the throat, and just after the "top" of the vane, the section containing the highest Mach numbers appears. The heat transfer is dependent on the local velocity, which is high in this area. This rapid acceleration causes the heat transfer to increase. Besides, the boundary layer in this region decreases, thus reducing the resistance to heat transfer. Coincidentally, this region corresponds with the deviations observed in Figure 6. After the high mach number region, the flow is transitioning before separating near the trailing edge. This is shown by a decrease followed by an increase in mach number.

As previously mentioned, the discrepancies on the suction side are connected to the numerical model, specifically the turbulence model. The shortcomings of the turbulence model arise in stagnation regions and regions with steep acceleration [39,40], both present in this study. The model tends to overpredict turbulence levels in these regions but still performs better compared to other turbulence models [28]. By including transition models to the simulations, the discrepancies could be reduced [41]. However, for the purpose of this study, transition models are not included in the simulations.

6. Comparison of Air and Steam

In this section, a comparison between air and steam as a cooling medium is presented. To better understand how the vane is affected by the cooling mediums, three cross-sectional planes are selected to examine the disparity at different locations. These planes are located at 25%-span, mid-span, and 75%-span, with the hub as a reference, shown in Figure 8.
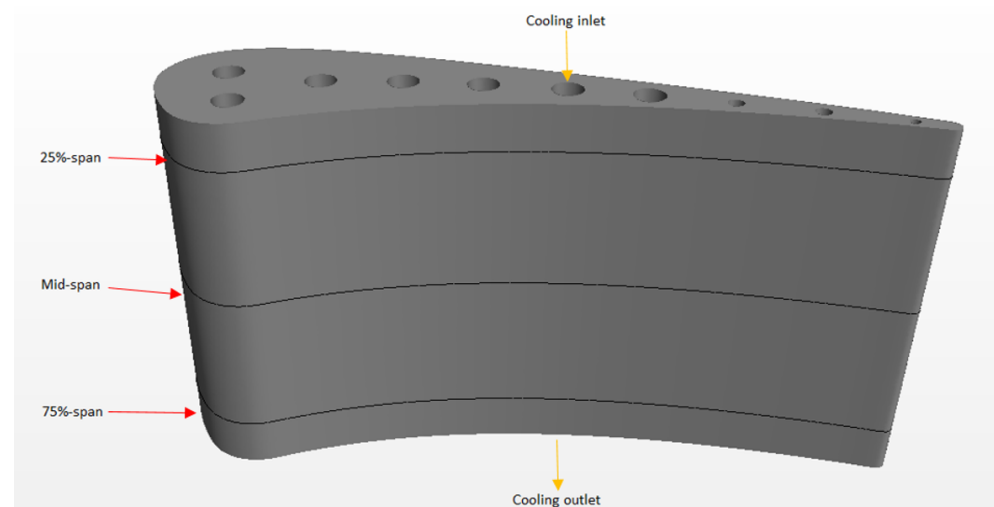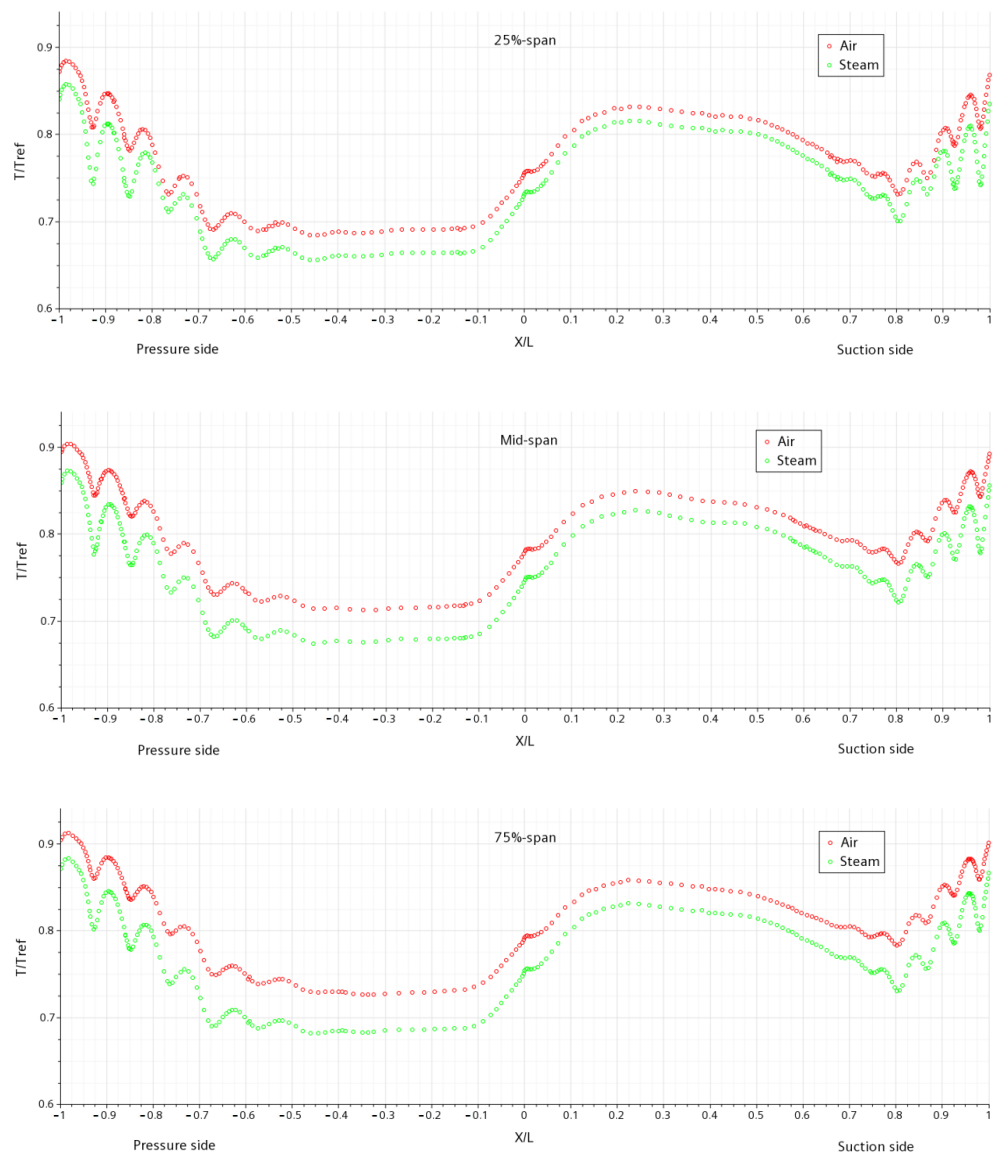

Figure 8. Location of the three cross-sectional planes used for comparison.

The normalised temperature distribution at these sections is displayed in Figure 9, which is used to study the thermal influence on the external wall of the vane. It is observed that the temperature profiles at the different cross-sections are reasonably consistent, as expected. Apart from the overall temperature, the only other noticeable difference is the fluctuations where X/L is between -1 and -0.5 on the pressure side and between 0.7 and 1 on the suction side. In all sections, the steam results show a steeper decrease and increase of temperature, and the variation between the bottom and vertex of the fluctuations are significant. This difference indicates that the cooling effects of steam are more significant than air. Besides, it is detected that the difference between the results increases from the hub to the shroud. The average difference between all data points increases from 3.89% to 4.87%; then, it increases to 5.29%. The total increase is 1.6%, which is equivalent to 13 K. This implies that the temperature rise along the vane is slower when steam is used, confirming the previous statement.
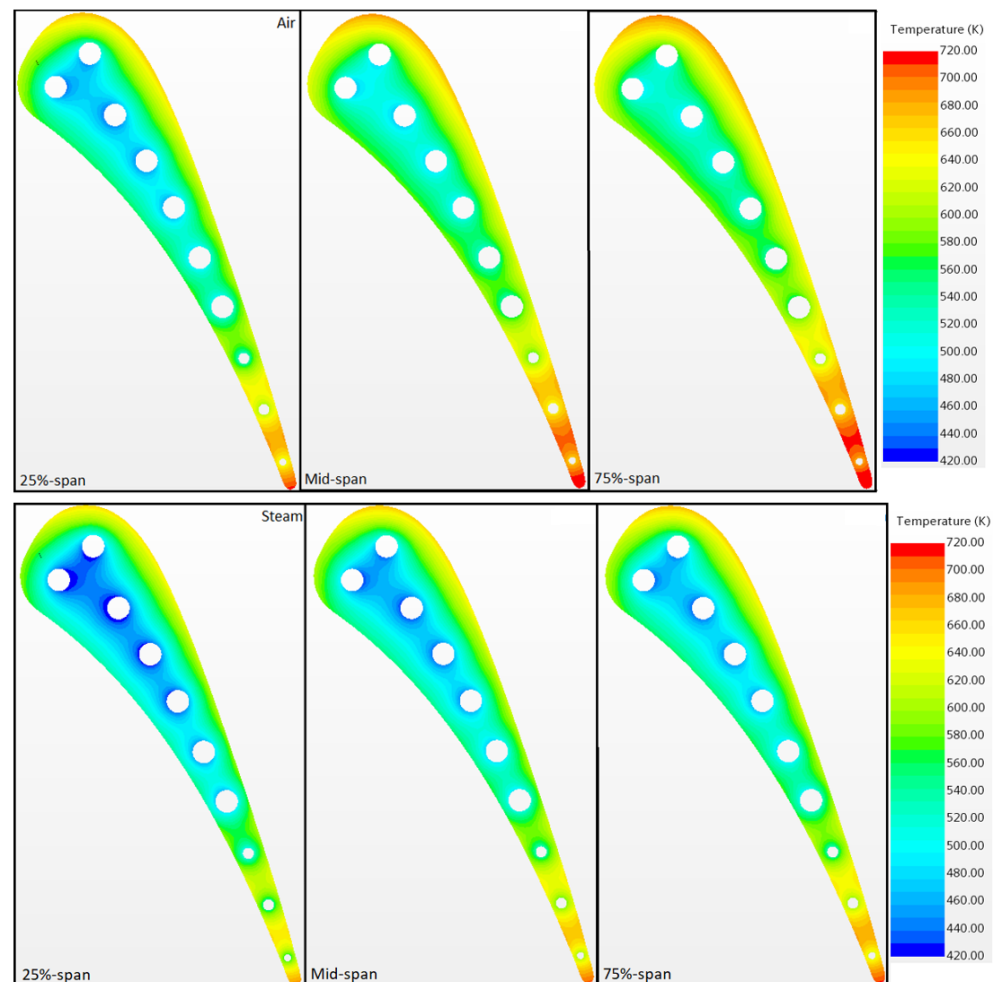
Figure 10 displays the temperature contours in the previously defined cross-sectional planes. It is useful to study these temperature contours to get a complete impression of the temperature in the vane. By comparing the air and steam contours, the previously established trend is apparent. The vane gets hotter as the distance from the hub is increased, and steam is the superior cooling medium. The temperature rise in the spanwise direction is due to a decrease in the cooling effect, caused by an increase in the coolant temperature. Additionally, some other details are noticed from this figure. It is observed that the heat transfer on the pressure side is lower compared to the suction side. This is displayed by the "cooler" areas stretching toward the pressure side. In addition, two areas of interest

become visible in this figure. Both the "top" of the vane and the trailing edge exhibits high temperatures, suggesting that these areas are prone to high thermal loads.

The static temperature distribution on the external surface of the vane is presented in Figure 11. It is observed that the maximum temperature, as earlier stated, appears near the trailing edge of the vane. This high temperature is due to the small diameter of the channels, low mass flow rate, and the thickness of the vane. The location of the cooling channels, especially near the trailing edge, is obvious, showing the effect of this cooling mechanism. It is noticed that the cooling channels exhibit wave-like behaviour, which is a result of the thermal energy transferred from the mainstream to the coolant along the axial direction. On the pressure surface, it is noticed that low-temperature zones are formed following the leading edge. This is due to the blade's profile, where the flow is fully developed, displaying a higher thermal resistance in these zones. As a final observation, steam is yet again proven to be the preferable cooling medium. In fact, the volume average temperature is 30 K lower when using steam.

Figure 9. Comparison of normalised temperature distribution at the three cross-sectional planes. The reference temperature is 811 K, as reported in [11].

Figure 10. Temperature contour comparison of the different cross-sectional planes.

When steam is used as the cooling medium, the temperature in the vane is reduced; however, the temperature in the external gas path remains unaffected. The exception of this is seen near the trailing edge of the vane, as shown in Figure 12. It is also observed that the temperature is slightly lower immediately after the trailing edge when steam is used. The steam reduces the temperature in the vane, which affects the hot gas stream near the external wall of the vane. This difference is hard to observe along the vane walls but is visible after the trailing edge when the flows are reattaching.

Most of the flow parameter in the external gas path is very similar, regardless of the cooling medium. One example of this is shown in Figure 13, where the pressure in the external flow is nearly identical for the two cases. From this figure, it is also noticed that the pressure in the cooling channels is lower when steam is used. In addition, the smallest cooling channels are observed to have a higher pressure. When the temperature is decreased, the pressure will also decrease. Since the smaller channels are more affected by the external hot gas path, the pressure becomes higher, as depicted in the figure.

Two other parameters which are influenced by the temperature are enthalpy and heat flux. The enthalpy in the cooling channels with the two cooling mediums is presented in Figure 14. It is shown that the enthalpy is increased when steam is used as a cooling medium. In addition, it is noticed that the enthalpy increases along the axial direction of the vane. Figure 15 is displaying the normalised heat flux at the mid-span of the vane. It is obvious that the heat flux is increased when steam is used as a cooling medium. Both of these parameters are greatly affected by the temperature difference between the hot gas

and the cooling medium. When steam is used as a cooling medium, the temperature is decreased. As a result, both the enthalpy and the heat flux is increased.
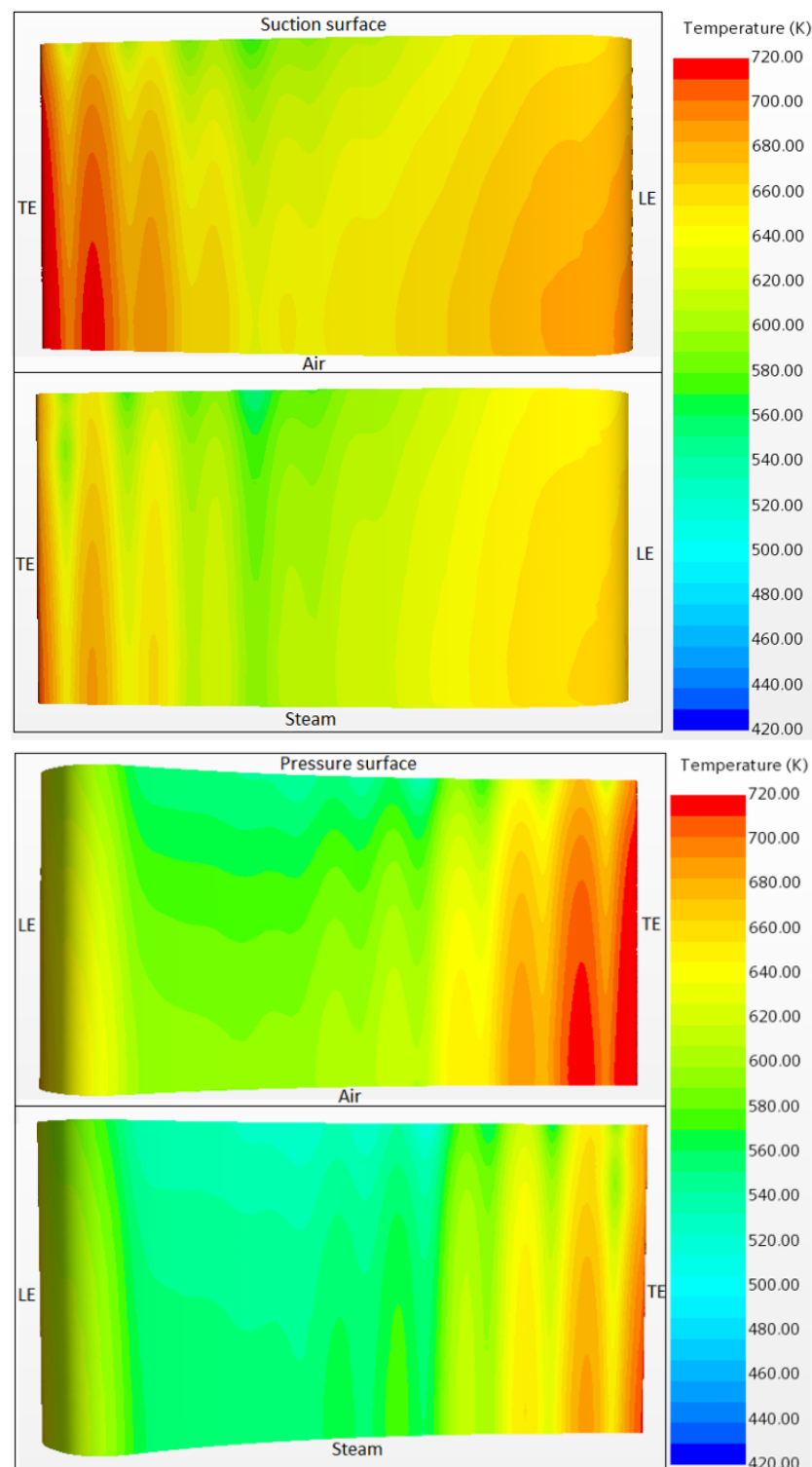

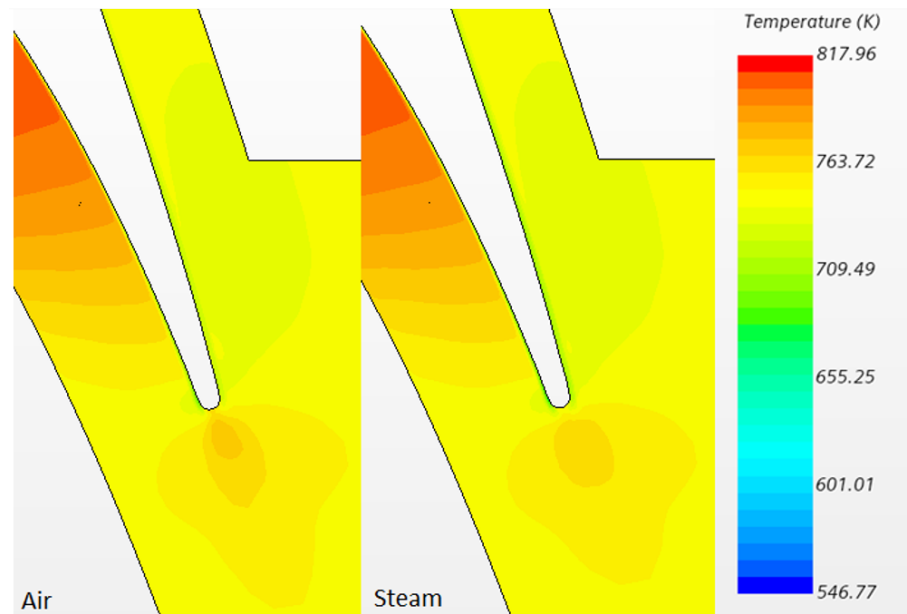**Figure 11.** Temperature contour comparison at the pressure and suction surface.

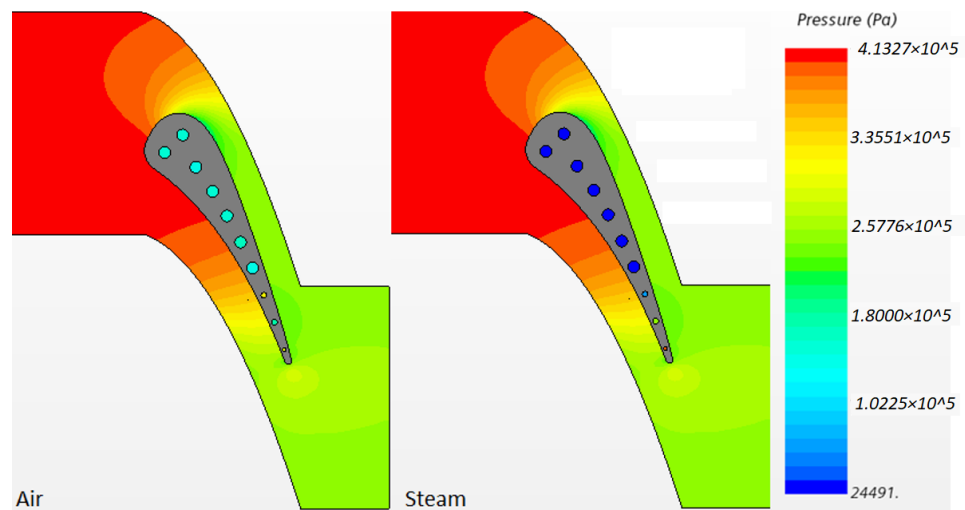**Figure 12.** Comparison of the external gas flow temperature near the trailing edge at mid-span.

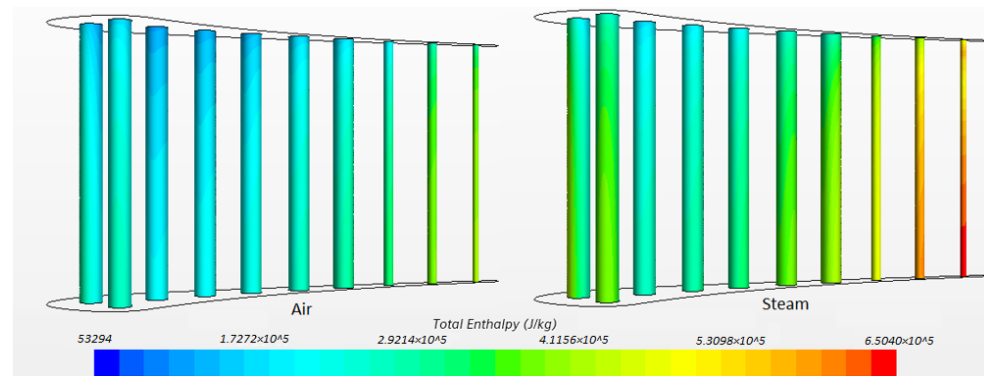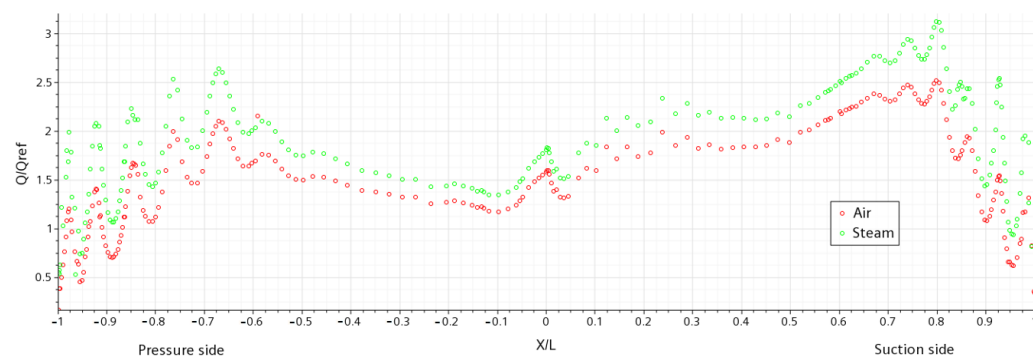**Figure 13.** Pressure contours of the fluid regions in the simulations at mid-span.

Figure 14. Comparison of the total enthalpy contours in the cooling channels. Colour bar is displaying the different enthalpy levels present in the figure.

Figure 15. Comparison of normalised heat flux distribution at mid-span. The reference heat flux is 100,000 W/m^2 and is selected to normalise the results.

7. Summary and Conclusions

Three-dimensional conjugate heat transfer analyses have been performed on the radially cooled NASA C3X turbine guide vane, using the RANS based SST $k - \omega$ turbulence model. The objective was to evaluate the effects of steam as a cooling medium compared to the traditional compressed air coolant. The computational model was validated against experimental results [11]. The aerodynamic and thermal characteristics were in good agreement with the experimental results, where the average relative difference was 1.39% and 3.78%, respectively.

The steam was proven to be the superior cooling medium, as expected. The temperature distribution of the two coolants displayed the same trends in the defined cross-sectional planes. Additionally, it was observed that the difference between the mediums increased along the axial direction of the vane. The average difference increased from 3.89% at the 25%-span to 5.29% at the 75%-span, which is equivalent to an increase of 13 K, solidifying steam as the preferable coolant.

Finally, it was shown that both the air- and steam cooled vane had some local areas with high temperatures. The low cooling effectiveness in these areas may lead to undesirable thermal loads and thermal stresses, contributing to a reduced lifespan of the vanes. Thus, further investigations are recommended to optimise the geometrical configuration and the mass flow rates of the cooling channels.

References

1. IEA. Global Energy Review 2019. Available online: https://www.iea.org/reports/global-energy-review-2019 (accessed on 9 March 2021).
2. McKinney, R.G.; Hoke, J.B. Aero gas turbine combustion: Metrics, constraints, and system interactions. *Gas Turbine Emiss.* **2013**, *38*, 3.
3. McDonell, V.; Klein, M. Ground Based Gas Turbine Combustion: Metrics, Constraints, And System Interactions. *Gas Turbine Emiss.* **2013**, *38*, 24.
4. Saravanamuttoo, H.I.; Rogers, G.F.C.; Cohen, H. *Gas Turbine Theory*; Pearson Education: Harlow, UK, 2001.
5. Langston, L.S. Turbines, gas. *Encycl. Energy* **2004**, *6*, 221–230.

6.   Konter, M.; Bossmann, H. Materials and coatings developments for gas turbine systems and components. In *Modern Gas Turbine Systems*; Elsevier: Amsterdam, The Netherlands, 2013; pp. 327–380. 381e.

7.   Naik, S. Basic Aspects of Gas Turbine Heat Transfer. In *Heat Exchangers–Design, Experiment and Simulation*; BoD—Books on Demand: Norderstedt, Germany, 2017; pp. 111–142.

8.   Wang, T. An overview of IGCC systems. In *Integrated Gasification Combined Cycle (IGCC) Technologies*; Elsevier: Amsterdam, The Netherlands, 2017; pp. 1–80.

9.   Ashby, M.F.; Jones, D.R. *Engineering Materials 1: An Introduction to Properties, Applications and Design*; Elsevier: Amsterdam, The Netherlands, 2012; Volume 1,pp. 351–363.

10.   Montomoli, F.; Carnevale, M.; D'Ammaro, A.; Massini, M.; Salvadori, S. *Uncertainty Quantification in Computational Fluid Dynamics and Aircraft Engines*; Springer: Berlin/Heidelberg, Germany, 2015.

11.   Hylton, L.; Mihelc, M.; Turner, E.; Nealy, D.; York, R. *Analytical and Experimental Evaluation of the Heat Transfer Distribution over the Surfaces of Turbine Vanes. Final Report Detroit Diesel Allison*; National Aeronautics and Space Administration, NASA Lewis Research Center: Cleveland, OH, USA, 1983.

12.   Hylton, L.; Nirmalan, V.; Sultanian, B.; Kaufman, R. *The Effects of Leading Edge and Downstream Film Cooling on Turbine Vane Heat Transfer. Final Report General Motors Corp*; National Aeronautics and Space Administration: Washington, DC, USA, 1988.

13.   Bohn, D.; Kruger, U.; Kusterer, K. Conjugate heat transfer: An advanced computational method for the cooling design of modern gas turbine blades and vanes. *Dev. Heat Transf.* **2001**, *8*, 58–108.

14.   Bohn, D.; Heuer, T.; Kusterer, K. Conjugate flow and heat transfer investigation of a turbo charger. *J. Eng. Gas Turbines Power* **2005**, *127*, 663–669. [CrossRef]

15.   York, W.D.; Leylek, J.H. Three-dimensional conjugate heat transfer simulation of an internally-cooled gas turbine vane. In Proceedings of the Turbo Expo: Power for Land, Sea, and Air, Vienna, Austria, 14–17 June 2004; Volume 36886, pp. 351–360.

16.   Facchini, B.; Magi, A.; Scotti Del Greco, A. Conjugate heat transfer simulation of a radially cooled gas turbine vane. In Proceedings of the Turbo Expo: Power for Land, Sea, and Air, Vienna, Austria, 14–17 June 2004; Volume 41685, pp. 951–961.

17.   Andrei, L.; Andreini, A.; Facchini, B.; Winchler, L. A decoupled CHT procedure: Application and validation on a gas turbine vane with different cooling configurations. *Energy Procedia* **2014**, *45*, 1087–1096. [CrossRef]

18.   Mousavi, S.M.; Nejat, A.; Kowsary, F. Optimization of turbine blade cooling with the aim of overall turbine performance enhancement. *Energy Equip. Syst.* **2017**, *5*, 71–83.

19.   Prapamonthon, P.; Yooyen, S.; Sleesongsom, S.; Dipasquale, D.; Xu, H.; Wang, J.; Ke, Z. Investigation of cooling performances of a non-film-cooled turbine vane coated with a thermal barrier coating using conjugate heat transfer. *Energies* **2018**, *11*, 1000. [CrossRef]

20.   Bak, J.G.; Cho, J.; Lee, S.; Kang, Y.S. Effects of inlet turbulence conditions and near-wall treatment methods on heat transfer prediction over gas turbine vanes. *Int. J. Aeronaut. Space Sci.* **2016**, *17*, 8–19. [CrossRef]

21.   Pope, S.B. Turbulent flows. *Meas. Science and Technol.* **2001**, *12*, 11. [CrossRef]

22.   Hahn, D.W.; Özisik, M.N. *Heat Conduction*; John Wiley & Sons: Hoboken, NJ, USA, 2012.

23.   Kays, W.M. Turbulent Prandtl number. Where are we? *ASME Trans. J. Heat Transf.* **1994**, *116*, 284–295. [CrossRef]

24.   Jones, W.; Launder, B.E. The prediction of laminarization with a two-equation model of turbulence. *Int. J. Heat Mass Transf.* **1972**, *15*, 301–314. [CrossRef]

25.   Wilcox, D.C. Reassessment of the scale-determining equation for advanced turbulence models. *AIAA J.* **1988**, *26*, 1299–1310. [CrossRef]

26.   Argyropoulos, C.; Markatos, N. Recent advances on the numerical modelling of turbulent flows. *Appl. Math. Model.* **2015**, *39*, 693–732. [CrossRef]

27.   Menter, F.R. Two-equation eddy-viscosity turbulence models for engineering applications. *AIAA J.* **1994**, *32*, 1598–1605. [CrossRef]

28.   Zheng, S.; Song, Y.; Xie, G.; Sunden, B. An Assessment of Turbulence Models for Predicting Conjugate Heat Transfer for a Tubine Vane with Internal Cooling Channels. *Heat Transf. Res.* **2015**, *46*. [CrossRef]

29.   Rossman, C.D.; Ricklick, M.A. Analysis of a Coupled Micro-and Triple-Impingement Cooling Configuration in the C3X Vane. In Proceedings of the 52nd AIAA/SAE/ASEE Joint Propulsion Conference, Salt Lake City, UT, USA, 25–27 July 2016; p. 4857.

30.   Goldsmith, A. *Handbook of Thermophysical Properties of Solid Materials*; Pergamon Press: Oxford, UK, 1963; Volume 5,

31.   Sutherland, W. LII. The viscosity of gases and molecular force. *Lond. Edinb. Dublin Philos. Mag. J. Sci.* **1893**, *36*, 507–531. [CrossRef]

32.   Cengel, Y.A.; Boles, M.A. *Thermodynamics: An Engineering Approach*, 6th ed.; (SI Units); The McGraw-Hill Companies, Inc.: New York, NY, USA, 2007.

33.   White, F.M.; Corfield, I. *Viscous Fluid Flow*; McGraw-Hill: New York, NY, USA, 2006; Volume 3.

34.   Burcat, A. Thermochemical data for combustion calculations. In *Combustion Chemistry*; Springer: Berlin/Heidelberg, Germany, 1984; pp. 455–473.

35.   Peric, M.; Ferguson, S. The advantage of polyhedral meshes. *Dynamics* **2005**, *24*, 504.

36.   Nikuradse, J. Laws of Flow in Rough Pipes. Available online: https://digital.library.unt.edu/ark%3A/67531/metadc63009/m2/1/high_res_d/19930093938.pdf (accessed on 28 May 2021).

37.   Knopp, T. Model-consistent universal wall-functions for RANS turbulence modelling. In Proceedings of the International Conference on Boundary and Interior Layers, Göttingen, Germany, 24–28 July 2006.

38. Chitale, K.C.; Rasquin, M.; Sahni, O.; Shephard, M.S.; Jansen, K.E. Boundary layer adaptivity for incompressible turbulent flows. *arXiv* **2014**, arXiv:1405.0620.

39. Oliver, A.; Lillard, R.; Schwing, A.; Blaisdell, G.; Lyrintzis, A. Assessment of turbulent shock-boundary layer interaction computations using the OVERFLOW code. In Proceedings of the 45th AIAA Aerospace Sciences Meeting and Exhibit, Reno, NV, USA, 8–11 January 2007; p. 104.

40. Jie, T.; Jie, J. Stress Limiter Consideration for k-omega Turbulence Models in Shock-Wave/Turbulent Boundary-Layer Interactions in Supersonic and Hypersonic Flows. In Proceedings of the 20th AIAA Computational Fluid Dynamics Conference, Honolulu, HI, USA, 27–30 June 2011; p. 3980.

41. Baratta, M.; Cardile, F.; Misul, D.A.; Rosafio, N.; Salvadori, S.; Forno, L.; Toppino, M. Redesign of the TG20 Heavy-Duty Gas Turbine to Increase Turbine Inlet Temperature and Global Efficiency. In Proceedings of the Turbo Expo: Power for Land, Sea, and Air, Online, 25–25 September 2020; American Society of Mechanical Engineers: St. Joseph, MI, USA, 2020; Volume 84089, p. V02CT35A033.